FFEMS Fatigue & Fracture of Engineering Materials & Structures
SPECIAL ISSUE CONTRIBUTION
doi: 10.1111/ffe.12329

Non-local high cycle fatigue strength criterion for metallic materials with corrosion defects

MOHAMED EL MAY[1], NICOLAS SAINTIER[1], THIERRY PALIN-LUC[1] and OLIVIER DEVOS[2]

[1]*Arts et Metiers ParisTech, I2M, CNRS, Talence 33405, France*, [2]*Universite de Bordeaux, I2M, CNRS, Talence 33405, France*

Received Date: 16 October 2014; Accepted Date: 27 May 2015; Published Online: 3 JULY 2015

ABSTRACT This paper proposes a volumetric high cycle fatigue (HCF) strength criterion able to quantify the influence of natural corrosion pits on the fatigue limit of a martensitic stainless steel with high mechanical strength. Elastic–plastic numerical simulations were performed for real pits geometry, identified by X-ray microtomography, to determine the local stress distribution. The analysis revealed that calculation of the fatigue strength for material with real (irregular) pit geometry required a non-local HCF strength criterion. Such model was proposed based on the Crossland equivalent stress averaged within a volume limited by a critical distance. This criterion was validated with HCF tests on specimens with natural corrosion defects of different sizes.

Keywords martensitic stainless steel; natural corrosion pit; non-local HCF strength criterion; X-ray microtomography.

NOMENCLATURE

a_{th} = dimension of non-damaging crack-like defect
f = loading frequency
d_c = critical distance of averaging stress
A = fracture elongation
A_s = aqueous solution with 0.1 M NaCl and 0.044 M Na_2SO_4
D = diameter of the idealized spherical geometry of corrosion defect
E = Young modulus
E_{imp} = imposed electrochemical potential
HCF = high cycle fatigue
HV = Vickers hardness
I_{max} = maximum of the current density achieved during pitting
$J_{2,a}$ = amplitude of the second invariant of the deviatoric stress tensor
K_t = theoretical stress concentration factor
N_f = number of cycles to failure
R = loading ratio
R_a = arithmetic surface roughness
SCE = saturated calomel electrode
UTS = ultimate tensile strength under quasi-static monotonic tension
V_a = material volume of averaging stress
Z_{def} = material volume affected by the defect
α, β = Crossland parameters
$\sigma_{0.2}$ = conventional yield strength with 0.2% plastic deformation
σ_a = stress amplitude
$\sigma_{a,nom}$ = nominal stress amplitude
σ_{eq} = equivalent stress of non-local criterion based on Crossland one
σ_{Cr} = equivalent stress of Crossland criterion
$\sigma_{H,max}$ = maximum value, during a load cycle, of the hydrostatic stress
σ^D = median fatigue limit under tensile loading at 10^7 cycles

Corrrespondence: M. El May. E-mail: mohamed.elmay@ensam.eu

Φ_{max} = diameter of the largest pit identified at the surface of the specimen
$\sqrt{area}$ = square root area of the defect projected onto a plane perpendicular to maximum principal stress

INTRODUCTION

Designing structures against corrosion and fatigue has become a key problem for many metallic structures evolving in complex environmental conditions of humidity (aeronautics, civil engineering, etc.). The combined effect of cyclic loading (fatigue) and corrosion reduce the fatigue strength.[1] Therefore, numerous publications[2–6] found that localized pre-corrosion defects increase the risk of fatigue crack initiation because of local stress concentration around defects. The effect of corrosion on high cycle fatigue (HCF) strength is strongly dependent on both the size and population of the defects.[5] Most of the theories about the HCF strength of metallic materials with geometrical defects deal with the definition of size sensitive fatigue criteria. Several fatigue strength criteria have been developed to account for the effect of a geometrical defect on the HCF strength.[7–12] These methods are often applied in the case of idealized geometries of defects (hemispheres ellipsoids, etc.) to evaluate the effect of geometrical defect due to castings process (shrinkage cavity, porosity). Two types of approaches exist:

- empirical approaches[8,9]
- non-local approaches[11–19]

Empirical approaches are based on the relationship between the fatigue limit and the defect size. In these approaches, the defect is considered as a crack (crack-like defect) with the existence of a non-damaging size (or threshold) of the defect (a_{th}). The empirical Murakami's relationship[8] gives a good estimation of the fatigue limit in case of uniaxial loading. This criterion was validated for a wide variety of materials (especially steels and cast irons).

Non-local approaches are based on the stress gradient/distribution around defects. The stress gradient criterion of Nadot *et al.*[13,19] takes into account the gradient of the Crossland equivalent stress. This gradient is computed along one direction of the component (where the gradient is maximum) and over a distance limited by the defect size ($\sqrt{area}$). Such methods are difficult to use on real defects with irregular geometries or on complex component geometry because stress gradient computation with these approaches require to define a direction for the stress gradient evaluation. Non-local HCF criterion with a volume averaging method is a second way to consider stress strain distributions especially in 3D. They predict the fatigue limit by assuming that the apparent reduction in fatigue strength for small defects is due to the fact that the damage processes occur over only a small material volume. This volume can be defined using a threshold stress,[15] an energy threshold,[11,12,18] or a critical distance threshold.[16,20] Taylor *et al.*[16,20] suggest that failure occurs if the average stress exceeds the endurance limit over some critical volume surrounding the 'hot-spot'. To simplify calculations, these methods were reduced to stress calculation at a single point, or averaged over a critical distance or area (2D or 3D). These approximations are referred by Taylor[16] as point, line, area and volume methods.

The purpose of this study is to propose a volumetric non-local HCF strength criterion able to account for real geometries and distributions of corrosion defects. These are considered as geometrical defects. Generally, the deterioration of the actual surface of a corrosion pit, for example, through hydrogen embrittlement could be taken into account. This effect was neglected in our work, because the duration of the pitting process is typically less than 2 min, which is much smaller than the characteristic time for natural hydrogen diffusion in metals.[21] Consequently, its influence on the fatigue limit should be small. [22]

MATERIAL AND EXPERIMENTAL PROCEDURE

Material

The material used in this work was a high-strength rolled martensitic stainless steel (X12CrNiMoV12-3) developed for aeronautic applications. Its chemical composition and mechanical properties under quasi-static monotonic tension are given in Tables 1 and 2. The microstructure of this steel is completely martensitic, as shown in Fig. 1 (residual austenite content is less than 1% in volume). Austenitic

Table 1 Chemical composition of the X12CrNiMoV12-3 stainless steel (wt%, Fe balance)

C	Cr	Ni	Mo	V
0.12	12	3	1.6	0.3

Table 2 Mechanical properties of the X12CrNiMoV12-3 stainless steel under monotonic quasi-static tension.

E (GPa)	$\sigma_{0.2}$ (Mpa)	A (%)	Hardness (HV)
211	1040	15	430

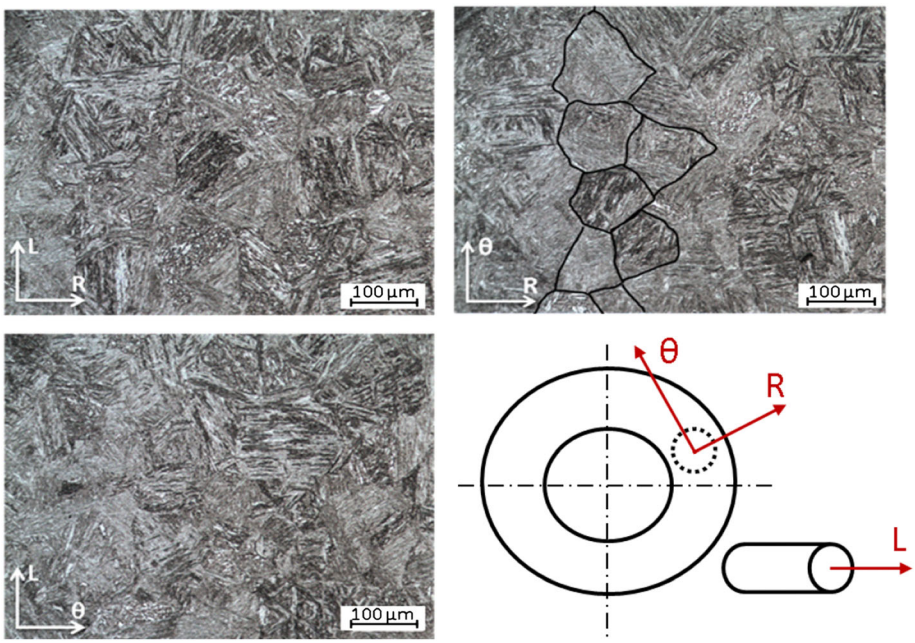

Fig. 1 X12CrNiMoV12-3 stainless steel: fully martensitic microstructure after heat treatment.

grains have an equiaxed structure and the grain size is approximately 100 µm (class 5, according to the ASTM E112-13 standard).

The electrochemical reactivity of the material was identified by a linear scan voltammetry without any mechanical loading (no cyclic neither static stress applied), in an aqueous solution (A_s) with 0.1 M NaCl and 0.044 M Na_2SO_4. Note that the free potential of the X12CrNiMoV12-3 steel without any mechanical load is approximately +0.1 V/SCE. The potential was applied from −1 V/SCE up to +0.6 V/SCE at a scanning rate of 0.01 V/s. The cathodic potential corresponding to the water reduction was chosen to reduce the passive oxide layer. Thus, an activation corrosion peak was observed around −0.4 V/SCE because of iron oxidation involved as a result of the passive layer dissolution. A well defined corrosion potential E_{corr} was measured at −0.44 V/SCE. When the potential was shifted to more anodic values, the current decreased until becoming slightly positive. This potential range corresponds to the passivation domain, extending from −0.25 to +0.3 V/SCE. The pitting domain corresponds to potential values greater than +0.3 V/SCE. In this region, the imposed electrochemical potential provokes the local dissolution of the passive film inducing local corrosion defects called pits.

Experimental procedure

Fatigue tests were carried out in air on smooth specimens, virgin specimens and pre-corroded ones. The pre-corrosion was performed in a corrosive aqueous solution A_s, using cylindrical specimens with 8 mm diameter. The arithmetic roughness (R_a) of the area of interest was less than or equal to 0.1 µm for all the specimens. Corrosion pits were obtained in the centre of 10 mm long gauge section. The rest of the fatigue specimen was protected with anticorrosion varnish. This process restricted the creation of defect in the area of interest. Corrosion pitting was carried out at an imposed electrochemical potential of 0.35 V/SCE or at 0.4 V/SCE according to the desired maximum pits size. To simplify the calculation of the pit size, we consider an idealized hemispherical geometry. This approximation is supported by optical observations and X-ray microtomography analysis with a voxel size of 1.4 × 1.4 × 1.4 µm. Figure 2 shows that the profile of the defect area projected onto a plane perpendicular to the applied nominal normal stress is similar to a hemispherical defect. However, the effect of the real geometry is investigated in the following.

Considering the fact that the fatigue limit is affected by the largest pit size, the classification of pre-corroded specimens was realized according to the maximum diameter, of the observed defect, at the surface. The characteristic pits size was defined by the geometric parameter ($\sqrt{area}$) proposed by Murakami. This parameter was calculated using the maximum apparent diameter (Φ_{max}) of the defect at the surface of the specimen observed by optical microscopy (Eq. (1)).

$$\left(\sqrt{area}\right)_{max} = \sqrt{\frac{\pi \Phi_{max}^2}{8}} \quad (1)$$

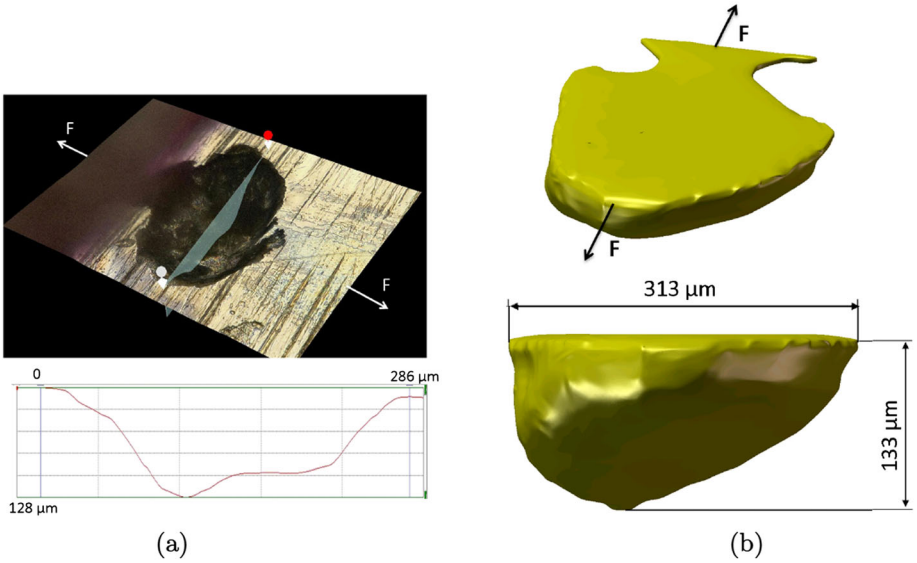

Fig. 2 Corrosion pits geometry observed by: (a) optical microscope and (b) 3D rendering of X-ray microtomography.

The stop criterion of the pre-corrosion process was the maximum current density achieved during pitting (I_{max}). Table 3 summarizes pitting tests on fatigue specimens. Four sizes ($\sqrt{area}$) of pits (equal to 17, 33, 64 and 188 µm) were considered to determine the Kitagawa diagram at 10^7 cycles.

To determine the experimental fatigue limit, HCF tests were carried out under axial loading and load control at 120 Hz with a resonant electromagnetic fatigue testing machine (Vibrophore type). This frequency was chosen so that failure at 10^7 cycles could be reached in a reasonable time. The stop criterion was a loading frequency drop of 0.7 Hz, corresponding to a technical fatigue crack with a typical surface length of 5 mm and a depth of 2 mm. After the fatigue tests, specimens were broken in monotonic tension after putting them in liquid nitrogen. Finally, the fracture surfaces of all the specimens were observed with optical and scanning electron microscope (SEM) to investigate the crack initiation mechanisms.

Table 3 Pitting test results on fatigue specimens

Specimen	E_{imp}(V/SCE)	I_{max}(mA/cm^2)	$(\sqrt{area})_{max}$ (µm)
1	0.4	0.18	19
2		0.2	17.2
3		0.19	17.8
4		0.22	15.8
5		0.21	14.5
6	0.4	0.31	29.8
7		0.32	30.8
8		0.29	33.6
9		0.27	33.1
10		0.33	33.7
11		0.3	31.4
12	0.35	0.53	66
13		0.58	69
14		0.49	60.9
15		0.47	61.7
16		0.52	67.8
17		0.46	63.4
18	0.35	0.76	207
20		0.82	200
21		0.8	182
22		0.79	188
23		0.81	194
24		0.77	196

RESULTS

Fatigue tests results

The fatigue strength at 10^7 cycles under fully reserved tension was determined in air on virgin and pre-corroded specimens with four controlled defect sizes. For the fatigue tests in air on virgin specimens, fatigue crack initiation sites are located on the specimen surface. No clear evidence of defects (pores, inclusions, etc.) was found at the crack initiation location. The SEM observations show that the fatigue cracks initiate at the surface around the largest corrosion defects in pre-corroded specimens.

An experimental Kitagawa diagram [9] representative of real corrosion pits (no micro-machining) was obtained (Fig. 3). This diagram is normalized by the ultimate tensile strength (UTS) for confidential reason. A minimum of five specimens by defect size was tested to identify the experimental fatigue limit at 10^7 cycles of the X13CrNiMoV12-3 stainless steel, using the short staircase method. The dimension of non-damaging defects is around 7 µm. The empirical Murakami fatigue criterion

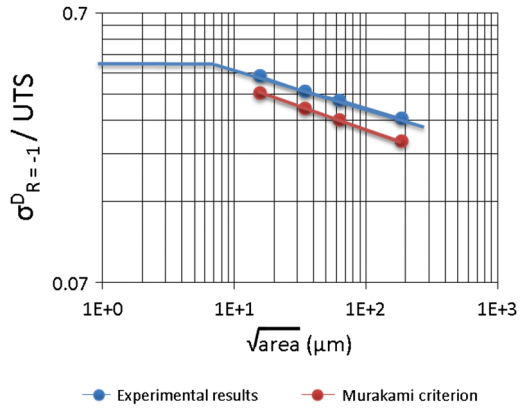

Fig. 3 Experimental Kitagawa diagram at 10^7 cycles under tension ($R = -1$) on pitted specimens.

for surface defects (Eq. (2)) [8,23] provides a conservative estimation of the experimental fatigue limit, but is difficult to apply when the local stress state is multiaxial.

$$\sigma^D = \frac{1.43(HV + 120)}{\sqrt{\text{area}}^{1/6}} \left(\frac{1-R}{2}\right)^{0.495} \quad (2)$$

Geometric parameters of corrosion defects

Corrosion defects have complex geometries and distributions. The fatigue strength of the corroded material can be affected by the interference phenomenon between neighbouring defects (Fig. 4). Therefore, it is necessary to consider this neighbouring effect on local stress–strain levels. Corrosion pits obtained in this study have approximately a hemispherical geometry and sometimes a crevice corrosion morphology. This one presents an apparent diameter at the specimen surface lower than the one measured below the surface. This geometry can modify the local stress distribution around the defect. To understand this effect, we propose to consider two geometrical parameters (Fig. 4):

- The distance h between the surface and the centre of the sphere to study the effect of crevice morphology of the corrosion pit on the local stress distribution;
- The distance d between two neighbouring defects to determine the threshold distance of interference between two defects (i.e. the distance below which the stress field around a defect is modified by another defect).

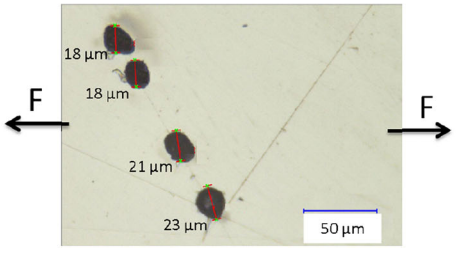

Fig. 4 Geometrical parameters of idealized corrosion defects.

FINITE ELEMENT MODELLING

In order to reproduce numerically the local stress–strain fields, in a reasonable computation time, a simplified geometry of the pre-corroded specimen is modelled. The simplification consists in explicitly modelling only the notch zone around the largest pit. The size of the representative volume is five times larger than the diameter of the pit to avoid any boundary effect. The finite element mesh of the modelled zone is obtained using tetrahedral finite elements, with quadratic interpolation (Fig. 5). The finite element calculations were carried out using an elastic–plastic model, with nonlinear kinematic and isotropic hardening. The parameters of the constitutive model were optimized using the experimental stabilized cyclic behaviour of the material. The numerical simulations were carried out with the ZeBuLoN FE software developed by Mines ParisTech, NorthWest Numerics and ONERA.[24]

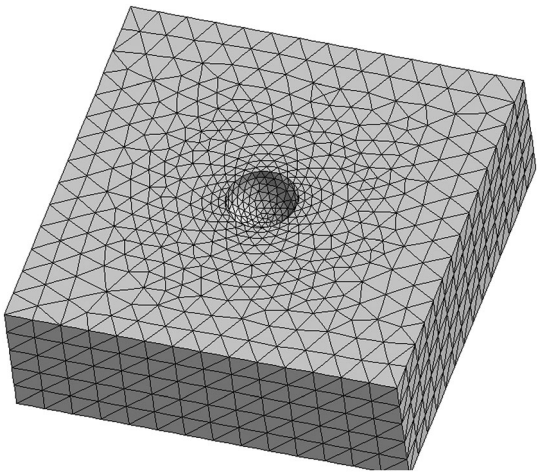

Fig. 5 Mesh of the modelled zone around the defect.

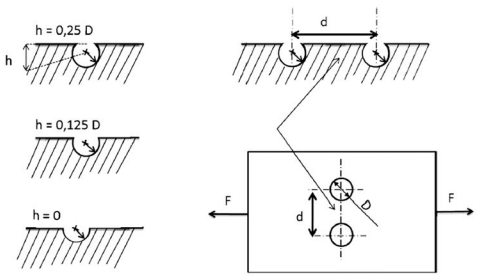

FATIGUE CRITERION

The purpose of this section is to present the volumetric approach based on the Crossland criterion proposed to describe the influence of defects.

Volumetric approach based on the Crossland criterion

The local Crossland criterion consists in a linear combination (Eq. (3)) of the amplitude of the second invariant of the deviatoric stress tensor (Eq. (4)) and the maximum value of the first invariant of the stress tensor over a cycle (hydrostatic stress) (Eq. (5)).

$$\sigma_{Cr} = \tau_{\mathrm{oct},a} + \alpha\, \sigma_{H,\max} \leq \beta \tag{3}$$

$$\tau_{\mathrm{oct},a} = \left(\max_{t_1} \left[\max_{t_2} \left[J_2 \left(\underline{\underline{\Sigma}}(t_1) - \underline{\underline{\Sigma}}(t_2) \right) \right] \right] \right)^{1/2} \tag{4}$$

$$\sigma_{H,\max}(M,t) = \max_{t \epsilon T} \left[\frac{1}{3} Trace \left(\underline{\underline{\Sigma}}(M,t) \right) \right] \tag{5}$$

The proposed criterion is based on the Crossland equivalent stress (σ_{Cr}) averaged in the influence zone of the defect (Z_{def}), within a material volume (V_a) limited by a critical distance (d_c) (Fig. 6).

$$\sigma_{\mathrm{eq}} = \max_{M \epsilon Z_{\mathrm{def}}} \left[\langle \tau_{\mathrm{oct},a} \rangle + \alpha \langle \sigma_{H,\max} \rangle \right] \leq \beta \tag{6}$$

At a surface defect, Z_{def} is the hemisphere centred on the defect with radius D equal to the defect diameter.

At a point M in Z_{def} , V_a is the sphere centred in M with radius d_c.

$$\langle \tau_{\mathrm{oct},a} \rangle = \frac{1}{V_a} \iiint_{V_a} \tau_{\mathrm{oct},a}\, dV \tag{7}$$

$$\langle \sigma_{H,\max} \rangle = \frac{1}{V_a} \iiint_{V_a} \sigma_{H,\max}\, dV \tag{8}$$

This criterion will be represented in the $(\langle \tau_{\mathrm{oct},a} \rangle, \langle \sigma_{H,\max} \rangle)$ diagram, called the non-local Crossland diagram. A Crossland danger coefficient C_d can be calculated, being proportional to the distance between the representative point in this diagram and the material threshold line which defines the fatigue limit. This danger coefficient (equation (9)) can be used to estimate the risk of crack initiation before 10^7 cycles:

$$C_d = \frac{\sigma_{\mathrm{eq}}}{\beta} \tag{9}$$

- no crack initiation for $C_d < 1$,
- crack initiation for $C_d \geq 1$.

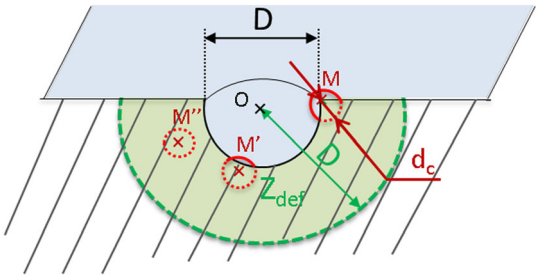

Fig. 6 Stress average volume around a critical distance d_c at all points M situated in the influence zone Z_{def}.

Criterion identification and validation for idealized hemispherical geometry

α and β parameters of the Crossland criterion were identified by using the fatigue tests in air on smooth specimens in tension, on the base material without any corrosion defect, for two loading ratios ($R = -1$ and $R = 0.1$).

The critical distance d_c was optimized at 7 µm using fatigue test results of only one size of defects ($\sqrt{\mathrm{area}} = 31\mu\mathrm{m}$). No link could be found between the value of d_c and the characteristic sizes of the material microstructure.

Figure 7 shows two Crossland diagrams for different pit sizes calculated using (a) the conventional Crossland criterion and (b) the proposed volumetric approach based on Crossland criterion with $d_c = 7\mu\mathrm{m}$. Scatter graphs represent all the values of $\tau_{\mathrm{oct},a}$ and $\sigma_{H,\max}$ calculated at the Gauss points of the mesh. The volumetric approach gives a good estimate of the HCF limit for different pits sizes (error less than 5%) compared with experimental results on pre-corroded specimens.

However, this approach was validated only in tension at a loading ratio equal to -1. The main difficulty in applying this volumetric HCF strength criterion is the obliged passage by a finite element analysis to identify the critical distance d_c. However, this criterion has the advantage to provide the capability to evaluate the fatigue strength of an industrial component with real geometry and complex configurations of defects. Indeed, no spatial direction has to be looked for to compute the stress gradient.

Effect of crevice morphology and the interference between nearby defects

Figure 8 shows two Crossland diagrams calculated using different configurations of pits: (a) crevice morphology and (b) neighbouring defects. These results showed a significant effect of the defect morphology (h parameter) on the median HCF limit at 10^7 cycles. The crevice morphology ($h > 0$) is the most critical in terms of fatigue crack initiation. The critical point for crack initiation according to this criterion is on the surface at the edge of

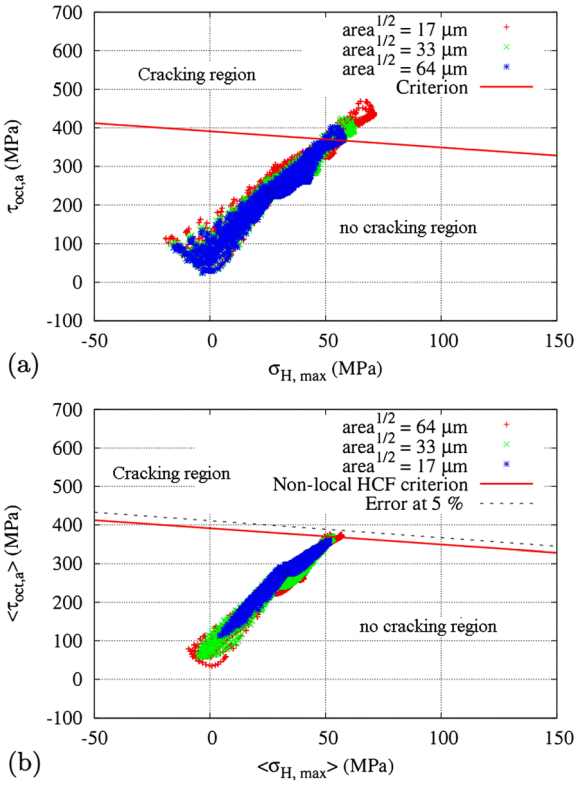

Fig. 7 Crossland diagrams for different pits sizes, using a hemispherical geometry ($h = 0$), loaded in tension ($R = -1$) at the experimental median fatigue limit at 10^7 cycles.

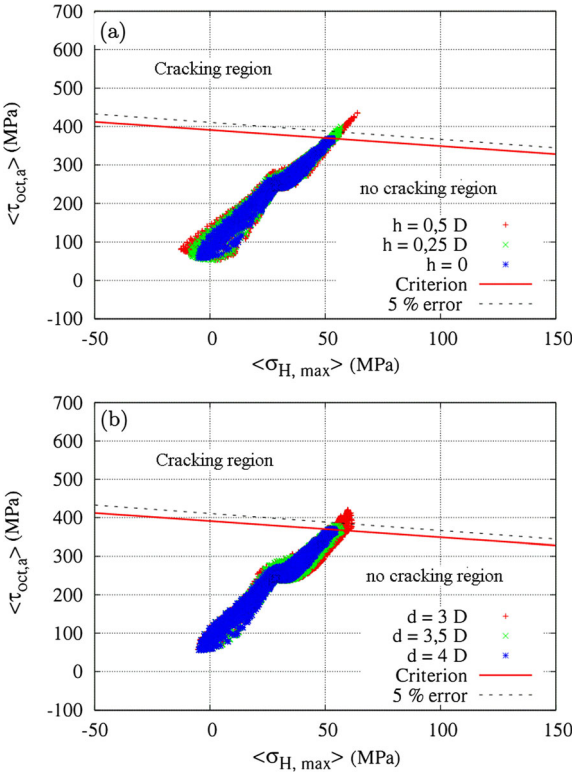

Fig. 8 Diagrams of the proposed volumetric approach based on the Crossland criterion (averaged with $d_c = 7\,\mu m$).

defect for h values larger than zero. This region corresponds to the highest value of the theoretical stress concentration factor K_t.

The study of the effect of the distance d between two identical defects located in the plane perpendicular to the loading direction shows that for a distance equal to three times the diameter of the defect, there is a higher risk of cracking than that observed with a single defect with the same size (Fig. 8). When the distance between the centres of two identical defects is greater than three times their diameter (D), there is no interference between defects.

Validation for real pit geometry

X-ray microtomography analyses were carried out to determine the real geometry of some pits, with a voxel size of $1.4 \times 1.4 \times 1.4\,\mu m$, on a specimen with the largest defect size used in this study ($\sqrt{area} = 188 \mu m$). This size was chosen to obtain an acceptable scan of the real geometry. This geometry has been processed by a software of computer-aided design to obtain a volume element containing a corrosion defect. The finite element mesh of the modelled zone was obtained using tetrahedral finite elements, with quadratic interpolation. Finally, elastic–plastic numerical simulations were performed with this real defect geometry, using the ZeBuLoN software, to determine the local stress distribution. The analysis revealed that calculation of the fatigue strength for

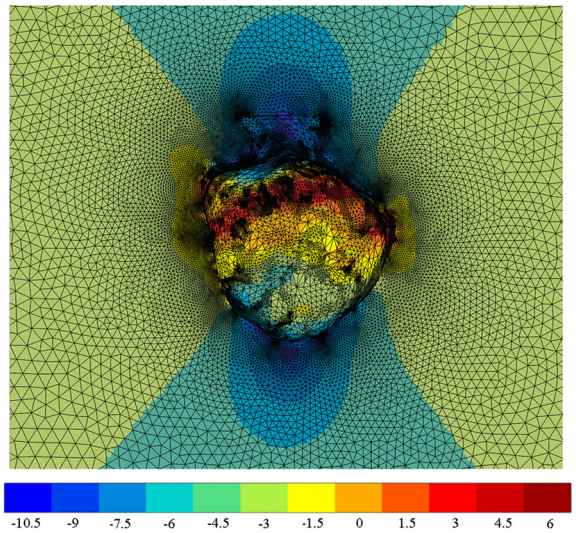

Fig. 9 Distribution around a real pit of the ratio (σ_{mises}/σ_H)) calculated at the maximum of the load cycle. This real pit geometry has been obtained by X-Ray microtomography.

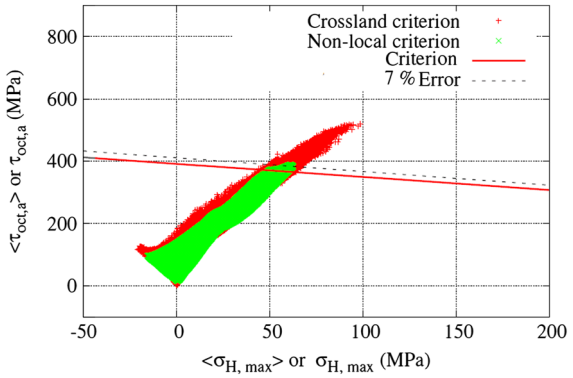

Fig. 10 Crossland diagram of real geometry of corrosion pit: comparison between local and volumetric approach based on the Crossland criterion.

material with real (irregular) pit geometry requires a non-local HCF strength criterion. The local distribution of stresses revealed a local multiaxial stress state, illustrated in Fig. 9, by plotting the ratio between the Von Mises equivalent stress and the hydrostatic stress. This ratio equals to 3 under uniaxial stress state and tends to infinite (+∞) for pure shear (deviatoric).

The median fatigue limit at 10^7 cycles for the same defect size was experimentally determined using the short staircase method. The volumetric approach of the Crossland criterion using the critical distance ($d_c = 7\,\mu m$), as identified previously, gives a good estimation of the fatigue limit (error less than 7%). Figure 10 illustrates the difference between the conventional Crossland diagram and the volumetric approach based on the Crossland criterion that is proposed in this study. The later allowing a good estimation of the HCF strength and the defect sensivity of the material.

CONCLUSIONS

A volumetric HCF strength criterion has been proposed in this paper to describe the influence of irregular geometries of real defects. This criterion is based on the Crossland equivalent stress that is averaged within a sphere of radius equal to a critical distance d_c. This proposal was validated with natural corrosion defects on X13CrNiMoV12-3 martensitic stainless steel tested under uniaxial fully reversed fatigue loading. Other material testing and multiaxial fatigue loading should be studied to confirm the prediction capabilities of the criterion.

Acknowledgements

This work was carried out in the framework of the ARCAM project, with the financial support of DGCIS, and Aquitaine, Auvergne and Midi-Pyrenees French regions. The authors thankfully acknowledge the industrial partners for the project, including Ratier-Figeac, Aubert et Duval, Olympus, and the academic partners at the Material Department of ICAM and the CIRIMAT (Toulouse University, France). The authors thankfully acknowledge the participation of Dr D. Bernard and Dr A. Chirazi from TOMOMAT, ICMCB institute (Bordeaux University, CNRS), to perform microtomography analysis.

REFERENCES

1 El May, M., Palin-Luc, T., Saintier, N. and Devos, O. (2013) Effect of corrosion on the high cycle fatigue strength of martensitic stainless steel X12CrNiMoV12-3. *Int. J. Fatigue*, **47**, 330–339.
2 Dolley, E. J., Lee, B. and Wei, R. P. (2000) The effect of pitting corrosion on fatigue life. *Fatigue Fract. Engng. Mater. Struct.*, **23**, 555–560.
3 Gruenberg, K. M., Craig, B. A., Hillberry, B. M., Bucci, R. J. and Hinkle, A. J. (2004) Predicting fatigue life of pre-corroded 2024-T3 aluminium. *Int. J. Fatigue*, **26**, 629–640.
4 Van Der Walde, K., Brockenbrough, J. R., Craig, B. A. and Hillberry, B. M. (2005) Multiple fatigue crack growth in pre-corroded 2024-T3 aluminium. *Int. J. Fatigue*, **27**, 1509–1518.
5 Kemanidis, Al. Th. Petroyiannis, P. V. and Pantelakis, Sp. G. (2010) Fatigue and damage tolerance behaviour of corroded 2024 T351 aircraft aluminium alloy. *Theoretical and Applied Fract. Mech.*, **43**, 121–132.
6 Palin-Luc, T., Pérez-Mora, R., Bathias, C., Domínguez, G., Paris, P. C. and Arana, J. L. (2010) Fatigue crack initiation and growth on a steel in the very high cycle regime with sea water corrosion. *Engng. fract. Mech.*, **77**, 1953–1962.
7 El-Haddad, M. H. (1979) Prediction of non-propagation cracks. *Engng. Fract. Mech.*, **11**, 573–584.
8 Murakami, T. (2002) *Metal Fatigue: Effect of small defects and non-metallic inclusions*. Ed. Elsevier: Oxford, Boston.
9 Kitagawa, H. and Takahashi, S. (1976) Applicability of fracture mechanics to very small cracks or the cracks in the early stage. *2nd Int. Conf. Mech. behavior of materials*, 627–631.
10 Nadot, Y., Ranganathan, N., Medez, J. and Béranger A. (1997) A study of natural crack initiated on casting defects by crack front marking. *Scri. Mater.*, **35**, 549–553.
11 Saintier, N., Palin-luc, T., Bénabes, J. and Cocheteux F. (2013) Non local energy based fatigue life calculation method under multiaxial variable amplitude loading. *Int. J. Fatigue*, **54**, 68–83.
12 Banvillet, A., Palin-Luc, T. and Lasserre, S. (2003) A volumetric energy based high cycle multiaxial fatigue criterion, *Int. J. Fatigue*, **25**, 755–769.
13 Gadouini, H., Nadot, Y. and Rebours, C. (2008) Influence of mean stress on the multiaxial fatigue behaviour of defective materials. *Int. J. Fatigue*, **30**, 1623–1633.
14 Morel, F. and Palin-Luc, T. (2002) A non-local theory applied to high cycle multiaxial fatigue. *Fatigue Fract. Engng. Mater. Struct.*, **25**, 649–665.
15 Sonsino, M. C., Kaufmann, H. and Grubišić, V. (1997). Transferability of material data for the example of a randomly loaded truck stub axle. *SAE Tech. Paper Series* (*970708*).
16 Taylor, D. Geometrical effects in fatigue: a unifying theoretical model. *Int. J. Fatigue*, **21**, 413–420.

17 Tovo, R., Benvenuti, E. and Livieri, P. (2004) Agradient formulation for the prediction of the static failure load of brittle notched components. *XV Congresso Italiano di Meccanica Computazionale*, *AIMETA*.
18 Palin-Luc, T. and Lasserre, S. (1998) An energy based criterion for high cycle multiaxial fatigue. *Eur. J. Mech. A/Solid*, **17**, 237.
19 Nadot, Y. and Billaudeau, T. (2006) Multiaxial fatigue limit criterion of defective materials. *Engng. Fract. Mech.*, **73**(1), 112–133.
20 Taylor, D. (2002) Geometrical effects in fatigue: a unifying theoretical model. XXXI Conf. of the Italian. Asso. of Stress Analysis (AIAS), Parma.
21 Ilin, D. N., Saintier, N., Olive, J-M., Abgrall, R. and Aubert, I., (2014) Simulation of hydrogen diffusion affected by stress-strain heterogeneity in polycrystalline stainless steel. *Inter. J. of Hydrogen Energy*, 2418–2422.
22 Forrest, P. G. (1962) Fatigue of metals. Preganon Press. 22.
23 Murakami, Y. (1996) Effect of small defects and inhomogeneities on fatigue strength: experiments, model and applications to industry. ECF 11, Poitiers, France, 31–42.
24 Besson, J., Leriche, R, Foerch R. and Cailletaud G. (1998) Object-oriented programming applied to the finite element method part ii. Application to material behaviours. *Revue Europeenne des Elements*, **7**, 567–588.